

1 **Mapping land degradation risk due to land susceptibility to dust emission and**
2 **water erosion**

3 Mahdi Boroughani^{1*}, Fahimeh Mirchooli^{1, 2}, Mojtaba Hadavifar³, Stephanie Fiedler⁴

4 ¹Research Center for Geoscience and Social Studies, Hakim Sabzevari
5 University, Sabzevar, Iran.

6 ²Sari agricultural Science and Natural Resources University, Sari, Iran

7 ³Environmental Sciences Department, Hakim Sabzevari University, Sabzevar,
8 Iran

9 ⁴University of Cologne, Institute of Geophysics and Meteorology, Cologne,
10 Germany

11 (Corresponding Author: m.boroughani@hsu.ac.ir)

12
13 **Abstract**

14 Land degradation is a cause of many social, economic, and environmental problems.
15 Therefore identification and monitoring of high-risk areas for land degradation are
16 necessary. Despite the importance of land degradation due to wind and water erosion,
17 the topic receives often relatively little attention. The present study aims to create a land
18 degradation map in terms of soil erosion caused by wind and water erosion of semi-dry
19 land. We focus on the Lut watershed in Iran encompassing the Lut Desert that is
20 influenced by both monsoon rainfalls and dust storms. Dust sources are identified using
21 MODIS satellite images with the help of four different indices to quantify uncertainty.
22 The dust source maps are assessed with three machine learning algorithms
23 encompassing artificial neural network (ANN), random forest (RF), and flexible
24 discriminant analysis (FDA) to map dust sources paired with soil erosion susceptibility
25 due to water. We assess the accuracy of the maps from the machine learning results
26 with the metric Area Under the Curve (AUC) of the Receiver Operating Characteristic
27 (ROC). The water and aeolian soil erosion maps are used to identify different classes
28 of land degradation risks. The results show that 43% of the watershed is prone to land
29 degradation in terms of both aeolian and water erosion. Most regions (45%) have a risk
30 of water erosion and some regions (7%) a risk of aeolian erosion. Only a small fraction
31 (4%) of the total area of the region had a low to very low susceptibility for land
32 degradation. The results of this study underline the risk of land degradation for in an
33 inhabited region in Iran. Future work should focus on land degradation associated with
34 soil erosion from water and storms in larger regions to evaluate the risks also elsewhere.

36 Key words: Desertification, Desert-dust sources, Risk susceptibility, Water-induced
37 soil erosion,

38

39 **Introduction**

40 Land degradation is one of the most pressing environmental issues around the globe.
41 Several aspects of this issue have been recognized by the United Nations Convention
42 (Gholami et al. 2019a). Land degradation can be driven by both water and wind, of
43 which the former can have a stronger impact on soil erosion in a short time (Gia et al.
44 2018). A total of 30% of global land area and three billion people are affected by land
45 degradation (Wieland et al., 2019). In Iran, it is estimated that land and water
46 degradation cost about US \$12.8 billion per year which is four percent of the total Gross
47 Domestic Product (GDP) (Emadodin et al. 2012). Therefore, spatial mapping of risks
48 of land degradation is necessary which can provide a basis to support managers and
49 policymakers in risk mitigation and adaptation to aeolian and water erosion.

50 Land degradation driven by aeolian erosion is a known problem (Shi et al. 2004). Dust
51 storms, which are a natural hazard, are associated with soil erosion. This phenomenon
52 has detrimental impacts on the Earth system, e.g., for food security (Boroughani et al.
53 2022), water supply (Duniway et al., 2019), human health (Moridnejad et al., 2015),
54 geochemical conditions (Gholami et al., 2020b), and the Earth's carbon cycle
55 (Gherboudj et al., 2017). Identifying dust sources as potential areas of dust emission is
56 therefore necessary for developing a better understanding of land degradation. Spatial
57 mapping of dust source susceptibility areas (DSSAs) is a crucial step for erosion
58 mitigation and watershed management.

59 In addition to soil erosion by wind, water-driven soil erosion is a known mechanism for
60 soil degradation. This kind of soil erosion is a known environmental threat and can
61 influence both terrestrial and aquatic systems (Halecki et al. 2018, Sun et al. 2014).
62 Therefore, knowing the spatial distribution of water-induced soil erosion susceptibility
63 areas (SESA) is also necessary.

64 Different approaches for identifying DSSAs exist, e.g., using meteorological data
65 (Yang et al. 2019), numerical modeling (Péré et al. 2018), and remote sensing (Jafari et
66 al. 2021). Remote sensing can provide worldwide information on aerosol properties
67 (Park et al. 2014). The present study uses Moderate Resolution Imaging
68 Spectroradiometer MODIS satellite images in combination with machine learning to

69 detect dust aerosols and map its susceptibility over the Lut Desert. Moreover, several
70 numerical models exist for predictions and risk evaluations of water-induced soil
71 erosion (Chicas et al., 2016, Gao et al., 2017, Anache et al., 2018, Gia et al., 2018,
72 Halecki et al., 2018), but none used machine learning to combine different
73 observational data sets for assessing soil erosion. Machine learning has emerged as a
74 subfield of data science and helps to better understand environmental problems
75 (Gholami et al. 2019b). It can integrate data from different sources to create forecasts
76 and discover patterns (Gholami et al. 2020a). In environmental sciences, algorithms
77 such as support vector machine, random forest (RF), artificial neural networks (ANN),
78 and multivariate adaptive regression spline have been applied, e.g., for groundwater
79 (Lee et al. 2017), gully erosion (Zabihi et al. 2018), sediment contamination (Mirchooli
80 et al. 2019), dust sources (Boroughani et al. 2020), landslides (Youssef and
81 Pourghasemi 2021), floods (Tehrany et al. 2014), and trace elements (Derakhshan-
82 Babaei et al. 2022).

83 However land susceptibility to soil erosion and dust emission has been assessed in
84 different and separate studies, it has attracted less attention to investigate both of them
85 in the same study. So, the novelty of this study lies in constructing an integrated
86 framework based on field survey, different environmental factors, and machine learning
87 algorithms to assess both of water erosion and dust emission.

88 This research is conducted to test some hypotheses including (1) the central and western
89 parts of the watershed are the highest susceptible areas to water erosion and aerosol
90 emission, respectively (2) NADI and land use are the most important factors for water
91 erosion and aolian emission and (3) Central areas are the most prone parts of the
92 watershed to these phenomena. Correspondingly, the aims of the current study are (1) to
93 assess the spatially resolved contribution of soil erosion by water and wind using three
94 machine learning algorithms, (2) determine the most important factor influencing water
95 and dust emission susceptibility and (3) to combine the findings into spatially resolved
96 information on risks for land degradation and recognize the hotspot area in terms of
97 water erosion and dust emission.

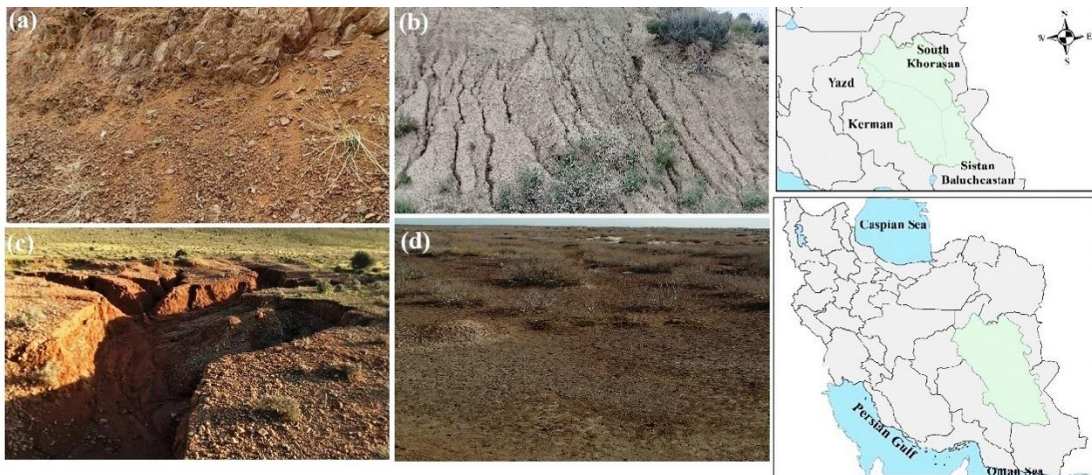
98

99 **2. Data and methods**

100 The focus of this study is on the Lut watershed situated in the east and southeast of Iran
101 covering an area of 206242 km² (28° 10' to 32° 30' N latitude and 55° 45' to 61° 15' E
102 longitude) and is marked in Fig. 1. This watershed include a great diversity of

103 topographic characteristics, with an elevation ranging from 124 to 4269m, and slope
104 ranging from 0 to 28.04 degree. In this region, southwest and northeast aspects have the
105 most frequencies (34% of the area). This watershed covers some parts of the South
106 Khorasan, Yazd, Kerman, and Sistan-Baluchestan Provinces of Iran. In addition,
107 several important cities and towns such as Birjand, Tabas, Bam located in the
108 watershed. Aridisols is the dominant soil order of the watershed in which it constitutes
109 40.1% of this region. The study watershed includes the largest desert of the country, the
110 Lut Desert. The region contributes to the increasing dust concentration in southwest
111 Asia (Ebrahimi-khusfi et al. 2021). This area is chosen to develop and test the methods
112 based on regional data on erosion observations with examples shown in Fig. 1a-d. It
113 underlines the impacts of land degradation that goes well beyond impacts on the natural
114 environment.

115



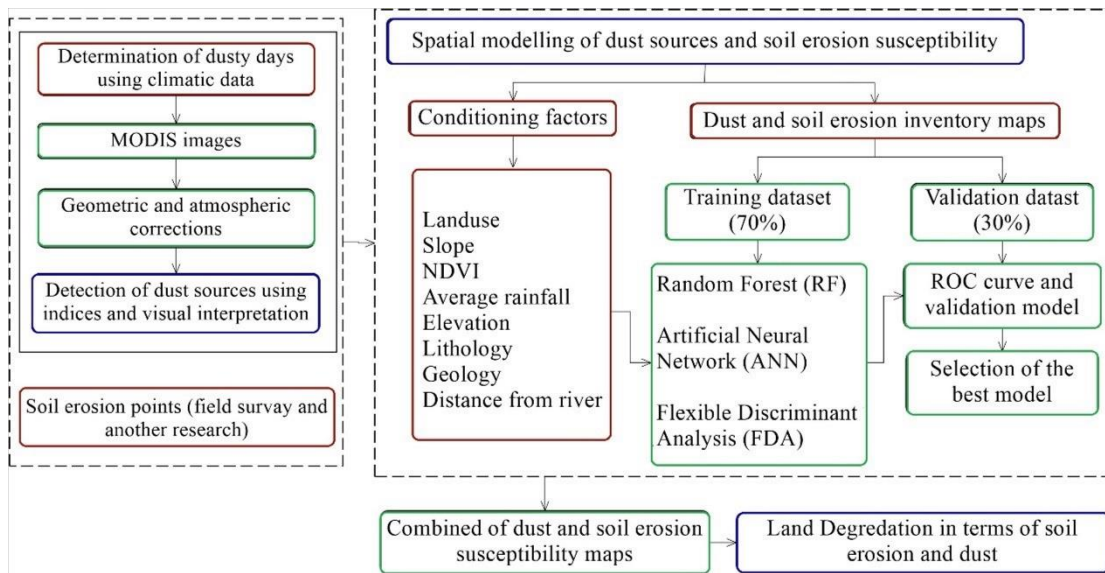
116

117 Fig.1 Geographical location of the study watershed. Green shading marks the Lut watershed. The Lut
118 Desert is located in the centre of the watershed. Settlements are primarily situated in the northern and
119 south-western parts. Example of soil erosion in the watershed are sheet erosion (a), rill erosion (b),
120 gully erosion (c), and wind erosion (d).

121

122 2. 1. Land degradation mapping

123 Our land degradation zonation consists of three main processing steps, graphically
124 depicted in Fig. 2. At first, spatial mapping of water erosion is conducted (section 2.1.1).
125 In the second step, spatial mapping of dust source susceptibility is carried out with
126 machine learning methods (section 2.1.2). In the last step, the patterns of water erosion
127 and dust source susceptibility are combined to identify risk areas of land degradation
128 (section 2.2.3).



130

131 Fig.2 Flowchart of inputs (red boxes), data processing (green boxes), and outputs
 132 (blue boxes) in the present study

133

134

135 2.1.1 water erosion map

136 Quantifying the erosion susceptibility of an area requires to determine a spatial
 137 distribution of observed water-induced soil erosion that can have different
 138 characteristics, e.g., gully erosion, rill erosion, and surface erosion. That information is
 139 extracted from data collected during an own field survey paired with previous research
 140 (Shit et al. 2020). In the previous research, a combination of consulting with provincial
 141 experts, satellite images, recent aerial photos, and field survey were applied to identify
 142 soil erosion. The aim of the field survey for the present study was to identify regions
 143 where sheet, rill, and gully erosion took place. This field survey was carried out in
 144 accessible parts of the watershed in April 2020. These accessible parts are mostly
 145 distributed around the cities (such as Bam, Ravar, Shahdad, Baravar, Birjand, Tabas,
 146 etc) with proper road access located in the watershed. The data set contains the type of
 147 water-induced soil erosion along with the geographical location using a Global
 148 Positioning System (GPS). A selection of the identified water soil erosions in the study
 149 region is shown in Fig. 1.

150 We translated the observations of the field survey into maps of non-degraded and
 151 degraded areas. These areas were plotted in an inventory map and prepared for further
 152 analysis, although not all desert areas are fully covered by the survey.

153

154 **2.1.2 Dust aerosol map**

155 The large desert area to be covered is a motivation for the use of satellite data for
156 estimating dust sources. We used MODIS images from the Terra (morning) and Aqua
157 (afternoon) satellites (Vickery and Eckardt, 2013) to identify dust aerosols. We define
158 dusty days, when the horizontal visibility is less than 2000 m for at least one hour during
159 the day based on available weather stations in Iran (Vickery and Eckardt, 2013;
160 Boroughani et al., 2021). According to the mentioned condition, more than 500 dusty
161 days were identified during 2010–2021 distributed over the stations in Birjand,
162 Zahedan, Kerman, Bam, Doostabad, Bisheh, Rafsanjan and Mighan. We pair the station
163 observations with satellite data to estimate the spatial extent of the dust aerosol plumes.
164 Due to the overpass of the Terra and Aqua satellites once per day, we acquired 28
165 satellite images from the MODIS sensor that during times when the weather stations
166 had documented dusty conditions in the ten-year period. For identifying pixels with
167 dust aerosols in these images, we calculate four different dust indices (BTD2931,
168 BTD3132, NDDI and D) for dust aerosol identification (Borroughani et al., 2020, 2021
169 Hahnenberger and Nicoll, 2014).

$$170 \quad B(T, \lambda) = \frac{2hc^2}{\lambda^5 \frac{hc}{(e\lambda kt - 1)}} \quad (1)$$

171 where $B(T, \lambda)$ represents the Planck equation at λ (μm), T is the BT (K), h is the
172 Planck's constant ($6.626 \times 10^{-34} \text{ m}^2\text{kg}^2\text{s}^{-1}$), k is the Boltzmann's constant (1.38×10^{-23})⁵, c
173 is the speed of light ($2.99 \times 10^8 \text{ ms}^{-1}$), and T is the temperature (Hao et al., 2007)
174

$$175 \quad T = \frac{hc}{\lambda k \ln(1 + \frac{2hc^2}{L\lambda^5})} \quad (2)$$

176 Using Planck's equation, the value of the temperature can be derived, where L is the
177 amount of radiance in the images (in $\text{Wm}^{-2}\text{sr}^{-1}\mu\text{m}^{-1}$).
178

$$179 \quad NDDI = (p_{2.13} - p_{0.469}) / (p_{2.13} + p_{0.469})$$

180 (3)

181

182 where $\square_{2.13}$ and $\square_{0.469}$ depict the reflectance value at the top-of-atmosphere at 2.13
183 and 0.469 μm , respectively (Qu et al., 2006)
184

$$185 \quad D = \exp\{-[rr \times a + (BTD - b)]\} \quad (4)$$

186 where rr shows the reflectance proportion among wavelengths of 0.54 μm and 0.86 μm
187 and BTD is the difference among the bands 11 and 12 μm ; a and b are constants taken
188 during the initial calibration (Eq. 1). (Qu et al., 2006; Miller, 2003; Hao et al., 2007;
189 Boroughani et al., 2020, 2021).

190 We compute false color maps using four combinations of channels (1: NDDI, B4, B3;
191 2: D, BTD_{2931} , NDDI; 3: D, BTD_{3132} , NDDI; and 4: BTD_{2931} , B4, B3) in ENVI
192 software. We choose these four different indices for cross-validating the presence of
193 dust aerosols. With each of these methods we see dust aerosol in different color and
194 qualities in the MODIS images over 28 days. After combining the four methods in the
195 software ENVI, we choose the method that shows the dust plume in the MODIS image
196 more clearly as the best method (Boroughani et al., 2020, 2022). This method is based
197 on a cone of dust diffusion seen in the processed MODIS images, where the apex
198 denotes the dust's source (Lee et al., 2009; Walker et al., 2009). Ultimately, the
199 inventory map of the dust aerosols in the Lut watershed was created.

200

201 **2.2. Identification of key factors controlling for aeolian and water erosion**

202 To develop DSSA and SESA, the identification and selection of appropriate dust
203 sources and soil erosion effective factors are necessary. The main factors affecting
204 DSSA and SESA were selected and constructed based on literature, available data and
205 geographical maps (Torabi et al., 2021; Zabihi et al., 2018; Boroughani et al., 2020;
206 Gholami et al., 2020a). The considered factors in this study included: elevation, land
207 use, slope of terrain, lithology, annual rainfall, distance from rivers, and distance from
208 roads, the Topographic Wetness Index (TWI), and Normalized Difference Vegetation
209 Index (NDVI). Various sources were used to gather data for these factors, introduced
210 in the following in more detail. All collected data were mapped to a horizontal grid of
211 1km resolution.

212 The shuttle radar topography mission (SRTM) images were used to create the digital
213 elevation model (DEM, , Fig 3c) (Ghorbanzadeh et al., 2018). The lowest and highest
214 elevation of the study area is 124 m in the centre of the desert and 3966 m at the western
215 and eastern margins of the study watershed, respectively (Fig. 3c). Vegetation cover
216 considerably supports soil conservation. Areas with low vegetation cover would be
217 more sensitive to both erosion by water and wind (Arabameri et al., 2019a; Gholami et
218 al. 2019b). Therefore, we use the Normalized Difference Vegetation Index (NDVI) to

219 assess the vegetation cover in the study area from MODIS images following
220 (Arabameri et al., 2019a; Boroughani et al., 2020):

$$221 \quad NDVI = \frac{NIR+R}{NIR-R}$$

222 Where R is the red (0.620-0.670 μm) and NIR is near-infrared bands (0.841-0.876 μm)
223 (Fig. 3d).

224 Annual rainfall (Fig. 3e) was obtained from Iran Meteorological Organization for the
225 period of 2000-2021. Mean annual rainfall was calculated using 40 different
226 meteorological stations located within or close to the watershed (Fig.3e). The inverse
227 distance weighting (IDW) interpolation method was applied to integrate rainfall over
228 the study area in the ArcGIS environment (Gholami et al., 2020a). Topographic
229 Wetness Index (TWI), which indicates the spatial distribution of areas of potential soil
230 saturation, is an effective factor to indicate water erosion including landslides and also
231 flooding (Arabameri et al., 2019b). TWI which determines the dry and wet zones
232 calculated as (Beven and Kirkby 1979):

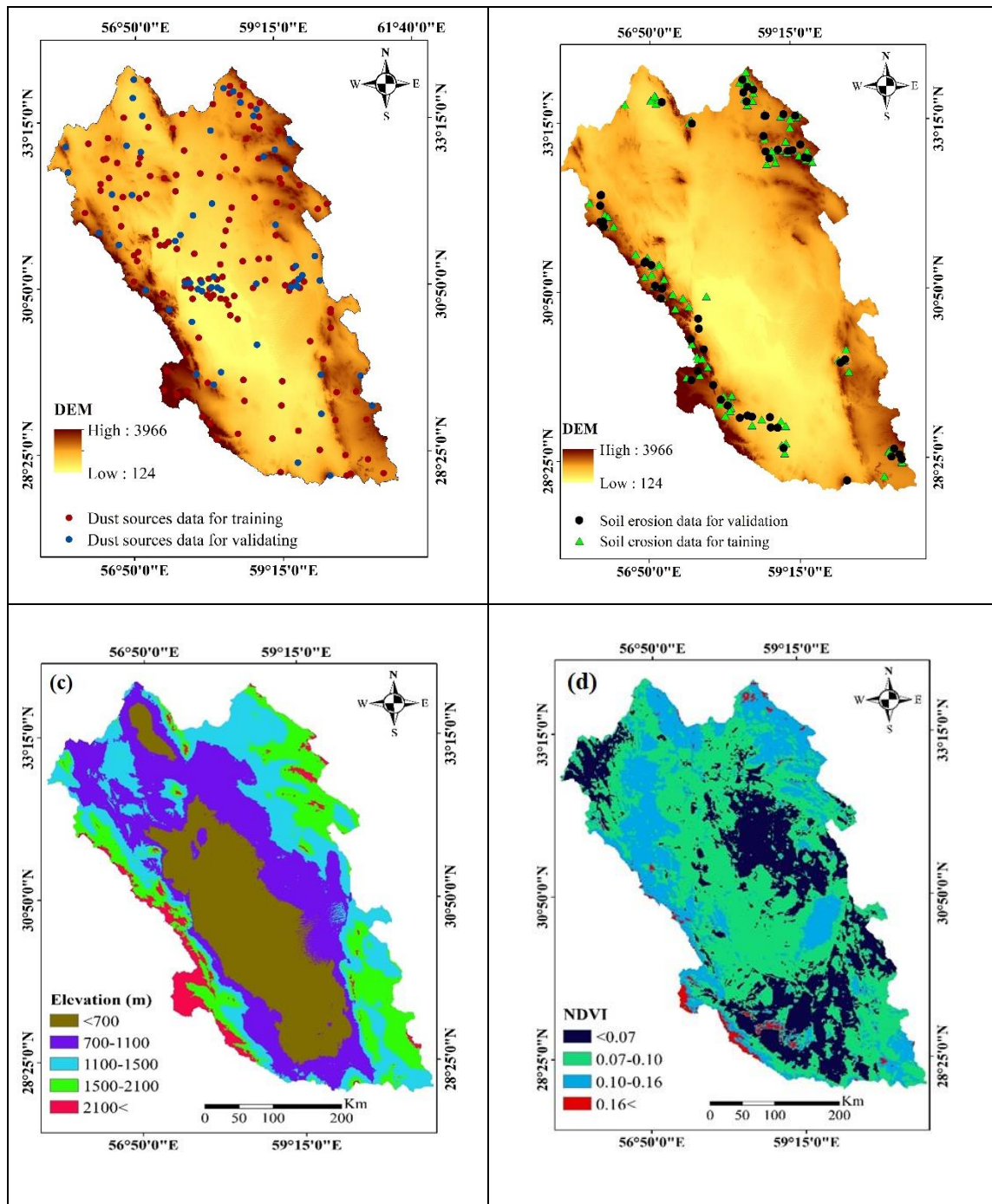
$$233 \quad TWI = \ln\left(\frac{\alpha}{\tan\beta}\right)$$

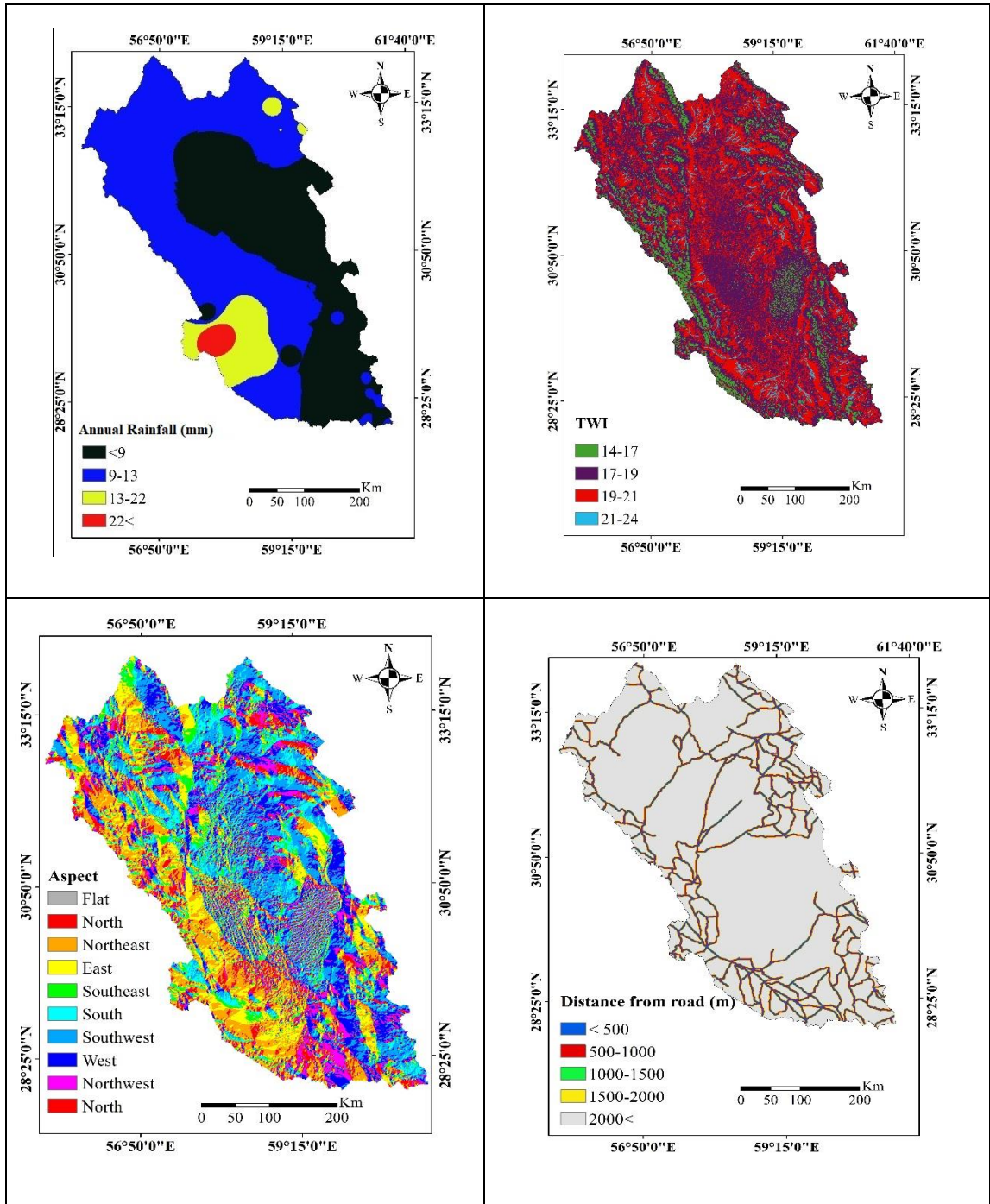
234 where α is the cumulative up-slope area from a point (per unit contour length) and β is
235 the slope angle at that point. This index was calculated in the SAGA-GIS environment
236 and classified into four groups viz. 14-17, 17-19, 17-21, 21-24 (Fig. 3f). The aspect
237 map was also generated using DEM and grouped into ten classes (Fig. 3 g). Distance
238 from road is an indicator of infrastructure development which influences soil erosion
239 and land degradation (Torabi et al., 2021). This factor is shown in five classes in Fig. 3
240 h. Distance from river is one of the most effective factors on water-caused erosion
241 (Amiri et al., 2019) which is classified into six groups (Fig. 3i).

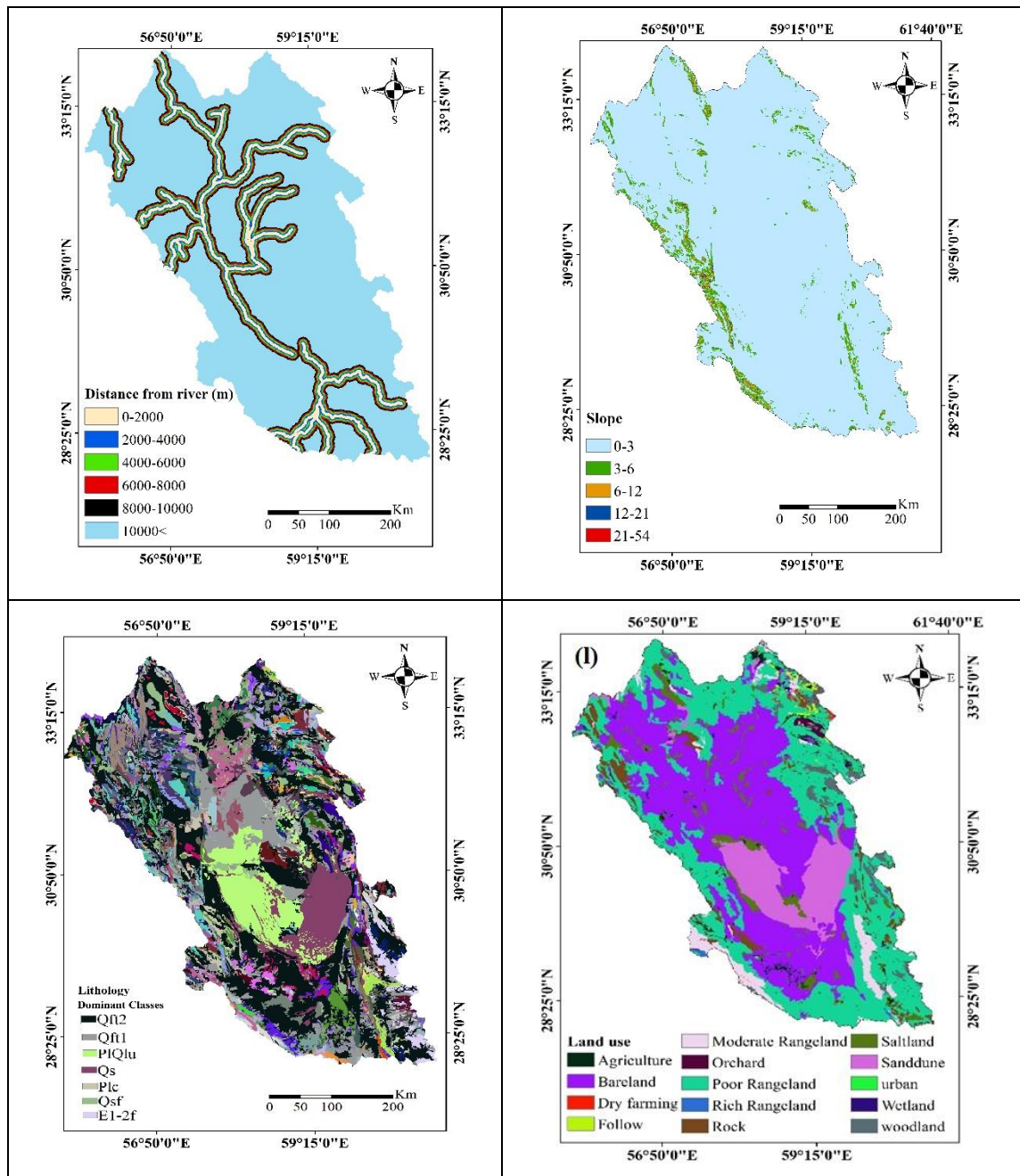
242 The slope map (%) was created using a Digital Elevation Map (DEM, Fig. j) and
243 classified into five groups including 0-3%, 3-6%, 6-12%, 12-21%, and 21-54%. The
244 lithology map indicates eleven different soil classes in the study area (Fig. 3k).

245 Land use and soil maps were obtained from base maps developed by the Iranian Forest,
246 Rangeland, and Watershed Management Organization (<https://frw.ir/>). In the study
247 region, there are fourteen land-use classes including wetlands, rangelands of three states
248 (poor, medium, and rich), dry farming, agricultural lands, urban area, fallow land, rock-
249 covered land, wetland, saltland, woodland, bare surfaces, and sand dunes (Fig. 3m). A
250 large percentage (83%) of the watershed area is covered by bare land, poor rangeland,

251 and sand dunes. All three land use classes are prone to wind erosion due to sparse or no
252 vegetation.







253
 254 Fig.3 Location of dust observation points for training and validation (a), water-induced soil erosion
 255 points for training and validation (b), and the conditional factors (Elevation (c), NDVI (d), Rainfall (e),
 256 TWI (f), Aspect (g), Distance from road (h), Distance from river (i), Slope (j), Lithology (k), Land use
 257 (l)) in the watershed.
 258

259 2.4. Spatial mapping of DSSA and SESA using machine learning algorithms

260 We combine the two susceptibility maps for DSSA and SESA to create the land
 261 degradation hazard map with regards to water- and wind-induced soil erosion. For both
 262 types of soil erosion, three machine learning models were constructed and applied. The
 263 land degradation susceptibility map was then created by synthesizing the results for

264 both soil erosion types in an ArcGIS 10.5 environment, and the land degradation
265 susceptibility was ultimately evaluated with four classes.

266 A wide range of machine learning algorithms has been applied for spatial mapping of
267 environmental phenomena in the past. The effective factors described in Section 2.2
268 and the inventory maps of water and wind erosion were used as the input of the machine
269 learning algorithms. In the present study, the algorithms of random forest (RF), artificial
270 neural network (ANN), and flexible discriminate analyses (FDA) were used to produce
271 DSSA and SESA maps. We choose three different algorithms to test the dependency of
272 the results on the method as a measure of uncertainty. The three algorithms are
273 described in more detail in the following.

274

275 **2.4.1 Random forest (RF)**

276 Random forest developed by Breiman (2001) is a machine learning algorithm for non-
277 parametric multivariate classification. RF builds multiple trees using a random selection
278 of the training dataset. The data not included are called out-of- bag (OOB) determines
279 the model accuracy using generalization error estimation (Breiman 2001). Diversity
280 among the classification trees increases using resampling the data with replacement and
281 also randomly change of predictors set during tree induction processes (Youssef et al.,
282 2016). Information from numerous decision trees has been combined in the RF
283 algorithm.

284 Generally, it is essential to define two parameters to run the RF model including the
285 number of trees (ntree) and the number of factors prepared from the data shown in Fig.
286 3 (mtry). The former is built while the RF model is running, while the latter is used in
287 the tree-building process. Both the number of trees and factors need to be optimized to
288 minimize the generalization error (Rahmati et al. 2016). The optimisation was done
289 through sensitivity tests.

290

291 **2.4.2 Artificial neural network (ANN)**

292 The artificial neural network (ANN) is a machine learning tool developed by imitating
293 human brain performances and making connections between inputs and outputs
294 (Sakizadeh et al. 2017). The human brain is mimicked in two ways: Firstly, obtaining
295 information and knowledge using a learning process, and secondly, storing knowledge
296 using synaptic weights. Therefore, ANN has been identified as the model that finds the
297 optimal solution for non-linear problems, such as dust source and soil erosion

298 susceptibility, by identifying patterns with conditioning factors (Ghorbanzadeh et al.
299 2019). In an ANN, a neuron is the smallest data processing unit which could make many
300 neural network structures and be used in research for different purposes. The standard
301 structure of ANN consists of three layers, namely, the input layer, the hidden layers,
302 and the output layer. The input layer consists of training data and conditioning factors
303 of dust source, the neurons in the hidden layer analyze the complex information
304 contained in the data, and the output layer is the maps of dust source susceptibility. In
305 this structure, the neurons across the same layer are not connected, but they are linked
306 with neurons in the previous and subsequent layers. In ANN, the algorithm determines
307 a weight for each input factor and a transfer function to build results (Kalantar et al.
308 2017).

309

310 **2.4.3 Flexible discriminate analyses (FDA)**

311 The modification of the linear regression model for the application to non-linear
312 problems is the purpose of FDA (Avand et al. 2021). Nonparametric regression models,
313 nonlinear discriminant analysis, and classification methods are combined into one
314 framework. This algorithm is flexible for non-linear classifications because non-linear
315 transformation is used and clusters are soft (Kalantar et al. 2020), here clusters for the
316 relationship between soil erosion and the predictor factors from Fig. 3. In this way,
317 variables in FDA are firstly aligned with the multivariate adaptive regression splines
318 (MARS) and then dimension reduction is performed (Kim and Kim 2021). FDA can
319 overcome the problem of linear discriminant analysis (LDA) and it is minimizing the
320 square average of the residuals (Mosavi et al. 2020), while linear regression is replaced
321 by nonparametric regression in FDA. Therefore, FDA has the potential to apply for
322 non-linear natural problems such as soil erosion, dust, flood, and landslide.

323

324 **2.5. Evaluation of machine learning algorithms**

325 In our DSSA and SESA assessment, 70% of point data are randomly selected for the
326 training dataset and 30% for model validation. The prediction accuracy of the machine
327 learning algorithms is assessed by comparing the DSSA map with the validation dataset
328 of dust sources. These data were extracted from MODIS images and some indicators
329 which were explained in section 2.1.2. The Receiver Operating Characteristic (ROC)
330 curve and the Area Under the Curve (AUC) are applied following past studies that used
331 these to test the prediction skill of a model for the occurrence or non-occurrence of the

332 studied phenomena (Naghibi et al. 2017). The AUC ranges from 0 to 1 in which the
333 models that better perform represent the AUC close to one.

334

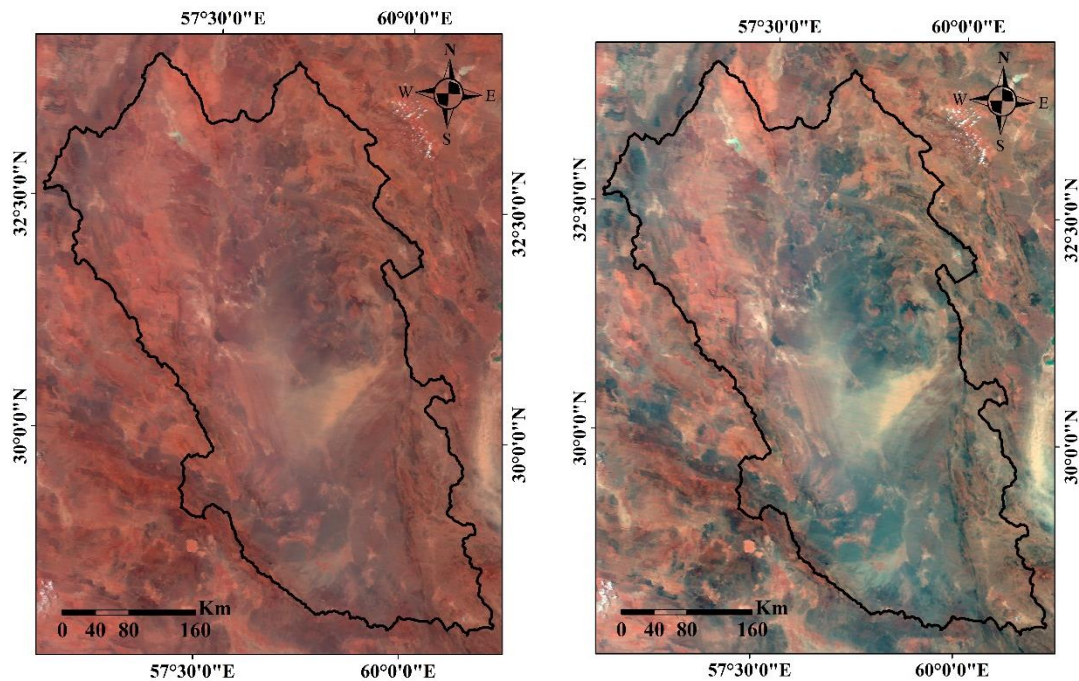
335 **3. Results and Discussion**

336 **3.1. Spatial distribution of DSSA**

337 **3.1.1. Dust aerosol detection**

338 An illustration of a dust storm seen in MODIS FCC satellite imagery over the Lut
339 watershed on August 7, 2019, is shown in Fig. 4. Following a visual analysis of the
340 images, we determined that the false colour combination (R: BTD2931, G: Band 4, B:
341 Band 3) is the best and applied it to 26 MODIS images of dusty days. As a result, the
342 Lut watershed's dust source locations were identified (Fig. 4).

343



344 Fig.4 The dust storm on 07 August 2019, as seen above is an example of the visual
345 inspection of a dust storm (a) MODIS true colour (Red: Band 5, Green: Band 4, Blue:
346 Band 3), and (b) enhanced MODIS satellite photos, (Red: BTD2931, Green: Band 4,
347 Blue: Band 3).

348

349 **3.1.2 The importance of conditioning factors for DSSA**

350 Since multicollinearity among factors has been identified as an obstacle to explaining
351 the results (Roy and Saha 2019), the Variance Inflation Factor (VIF) was calculated to
352 assess the relationships among conditioning factors. This was conducted because
353 multicollinearity among factors will decline the accuracy of the models (Arabameri et
354 al. 2019b). In the present study, VIF values for DSSA mapping range from 1.05 to 1.57
355 which illustrated no collinearity among the eight factors. Therefore, no exclusion was
356 applied and all factors were considered in successor calculations and modeling.

357 The importance and impact of each factor depend on the machine learning algorithms.
358 The result of DSSA mapping using RF showed that NDVI, elevation, land use, and
359 lithology had the greatest degree of effect among conditioning factors. Land use and
360 NDVI as an index of vegetation cover proved to have a controlling impact on wind
361 erosion and dust emission (Gholami et al., 2020). Elevation is an effective factor for
362 DSSA in which lowlands have higher impacts than highlands. This was confirmed by
363 other studies such as Darvand et al., 2021. Lithology is another important factor in this
364 watershed since dust emission is mostly occur in the sensitive lithology rather than
365 resistant ones (Sissakian et al., 2013). Overall, the impacts of these factors on DSSA
366 have been proved by previous investigations (Gholami et al. 2020a, 2020b). Other
367 factors such as the distance from rivers, rainfall, and slope were identified as rather
368 weak predictors, respectively. These findings agree with other research (Boroughani
369 and Pourhashemi 2020, Darvand et al. 2021).

370 The FDA approach showed that however elevation, NDVI, and land use had the highest
371 effects on dust sources susceptibility, other factors had no impact on DSSA. Similarly,
372 with ANN, elevation, NDVI, and land use were identified as the three most effective
373 factors, and other factors were weaker predictors rather than formers. However these
374 two models of FDA and ANN provide similar results in term of the importance of
375 conditioning factors, FDA could be used rather than ANN because of its higher
376 accuracy which is shown in the next section.

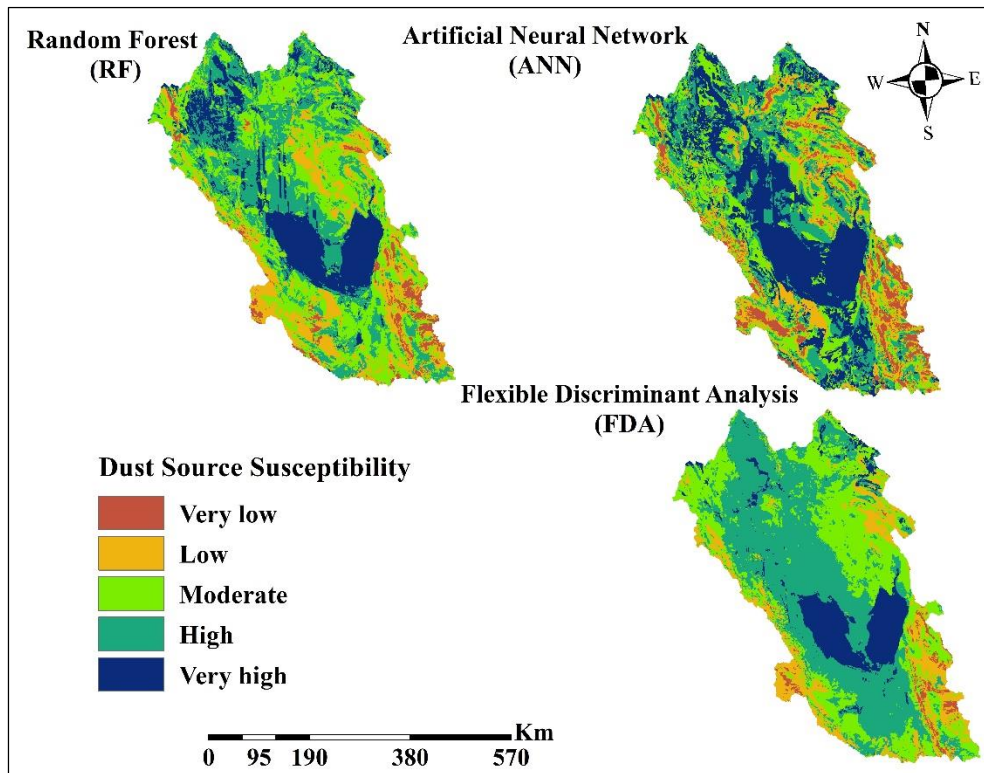
377

378 **3. 1. 3 Spatial distribution of dust source susceptibility**

379 The dust source susceptibility (DSS) maps created by RF, FDA, and ANN are classified
380 into five risk classes (very high, high, moderate, low, and very low) shown in Fig. 5.
381 These classes are set as in earlier studies (Mosavi et al., 2020; Boroughani,
382 Mohammadi, Mirchooli, & Fiedler, 2022). The results of the model evaluation using
383 ROC indicates that the RF model with an accuracy of 75.0% provides the most accurate

384 outputs. FDA and ANN had similar performances with the accuracy of 71.7% and
385 70.7%. In terms of True Skill Statistic (TSS), similar results have been obtained in
386 which RF with an accuracy of 45.8% had again the best performance in comparison to
387 FDA (32.4%) and ANN (35.8%). In this way, RF introduces different priorities for the
388 effective factors in comparison with FDA and ANN. RF proposes NDVI, elevation,
389 land use, and lithology as the most important factors, while FDA and ANN suggest
390 elevation, NDVI, and land use as the most influencing factors. The dominance of
391 NDVI, elevation and land use as the most effective factors for DSS is consistent with
392 the understanding of dust source locations that are typically found in topographic
393 depressions with sparse or no vegetation. The DSSA map from RF was selected for
394 further analysis due to the highest accuracy, although the differences between FDA and
395 ANN are in the statistical sense relatively small. According to the DSSA maps, 29%
396 and 17% of the watershed were classified as areas of high and very high DSSA, i.e.,
397 almost half of the study area. Only 4% and 16% of the watershed have a very low and
398 low susceptibility to soil erosion through winds, respectively. The spatial extent of high
399 and very high risk areas from RF is smaller than the ones obtained by ANN and FDA.
400 In all three maps, it can be seen that the biggest potential for dust emission is located in
401 the central parts (Lut Desert) of the watershed. These results are consistent with other
402 research, indicating that RF allows more detailed spatial mapping of dust source
403 susceptibility compared to other machine learning algorithms (Rahmati et al. 2020,
404 Gholami et al. 2019b, Darvand et al. 2021).

405



406

407

Fig. 5 Dust sources susceptibility area (DSSA) based on random forest (RF), artificial neural network (ANN), and flexible discriminate analyses (FDA)

408

409

410

As mentioned before, the watershed is one of the key regions with dust concentration in southwest Asia. Spatial distribution of dust sources in this region is a key roadmap for preventive and adaptive measurement. This would reduce dust emission across the watershed, region, and even other near countries.

413

414

415 3.2. Soil erosion susceptibility map

416 3.2.1 Relative influential conditioning factors for SESA

417

There are some differences in the contributions of influential factors among models. So that, RF indicates that rainfall, TWI, slope, elevation, land use, and geology are the most important conditioning factors. Considering this watershed located in arid region of Iran, rainfall and TWI play decisive and crucial role in soil erosion among them. TWI which indicate soil moisture and water-saturated area (Silva et al., 2023) has been also identified an effective factor for different kinds of soil erosion such as rill-interrill, gully, and piping erosions (Sholagberu et al., 2017; Hosseinalizadeh et al., 2019). Slope influences also soil erosion rate through effecting on runoff velocity, vegetation cover, and soil type (Avand et al., 2022). This conditioning factor has been also reported as

425

426 one of the most influential factor in most studies (Sholagberu et al., 2017; Pournader et
427 al., 2018; Lei et al., 2020). Moreover, distance from roads and rivers were recognized
428 as the least important factors. These findings of the impact of conditioning factors for
429 SESA are similar in other regions (Arabameri et al. 2019a, Hosseinalizadeh et al. 2019).
430 For ANN, TWI, slope, and land use were the most effective factors for prediction which
431 is followed by NDVI, land use, and distance from the river. The results from FDA
432 indicated that the most important conditioning factors are TWI, slope, and elevation,
433 geology, and NDVI. TWI has an important impact on SESA in all three models. This
434 is because the study watershed predominates with low slopes and elevations. The
435 opposite result of this finding was obtained by Silva et al., 2023.

436 A large area of the watershed is land with typically little rain and vegetation cover such
437 that bare soil is the main physical attribute in the watershed. This kind of surface is
438 known to be prone to water-induced soil erosion, when rain events occur. The erosion
439 can be particularly pronounced over slopes. This understanding is consistent with all
440 algorithms pointing to a major role of TWI and slope for SESA.

441 Some environmental factors (rainfall, TWI, slope, elevation, and geology) influence
442 SESA more than DSSA. Land use as a human-induced conditioning factor, however,
443 affects both SESA and DSSA, which underlines the importance of land-use planning
444 and management.

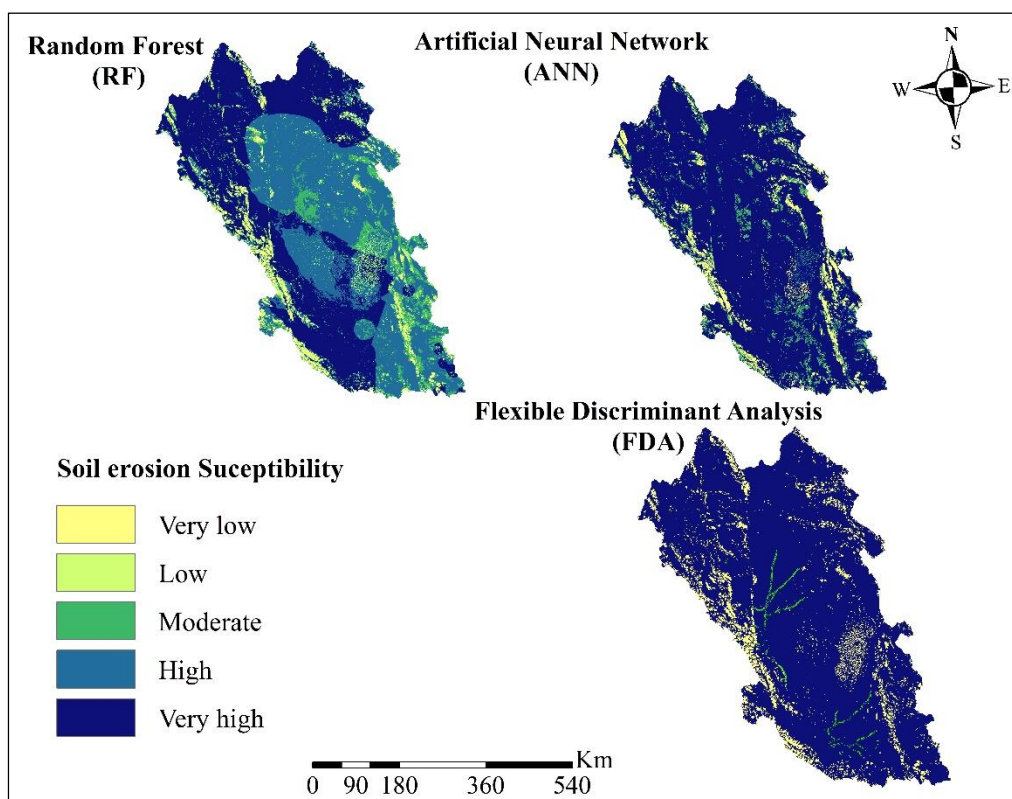
445

446 **3.2.2. Spatial modeling of SESA**

447 Fig. 6 shows the SESA predictions from the three machine learning algorithms,
448 classified by the soil erosion risk in the ArcGIS environment. Validation of the three
449 machine learning algorithms highlights that RF was again the most reliable algorithm
450 amongst the three, indicated by the best prediction rate. Based on ROC, RF yields a
451 94% accuracy for SESA (Fig. 6c). The ROC coefficient of ANN and FDA were slightly
452 lower, but still high with an accuracy of 91% and 89%, respectively. In the case of the
453 TSS index, better performance was obtained again for RF (89%) rather than ANN
454 (78%) and FDA (78%). High performance of RF model in classification issues is related
455 to its potential to handle big datasets and apply large number of conditioning factors
456 (Naghibi et al., 2018). In addition, Rahmati et al., 2020 states that high accuracy of RF
457 is the results of several advantage of this model such as iterative nature and preventing
458 problems by overfitting (Rahmati et al., 2020).

459 The majority of the land in the watershed (81%) has a high and very high risk for water-
 460 induced soil erosion by RF. This is slightly lower than for ANN and FDA which
 461 classified 85% and 89% of the watershed as high and very high susceptible areas. The
 462 high and very high susceptible areas for water-driven soil erosion are mostly located in
 463 the north and south-west parts of the watershed. The high and very high susceptible
 464 areas have socio-economic implications, particularly because most settlements and
 465 cities of the watershed are located in the same regions. This can mean that human
 466 activity is a contributing factor to the water-induced soil erosion. Mutually, intensified
 467 soil erosion might lead to migration of resident people to other places and even other
 468 countries.

469



470

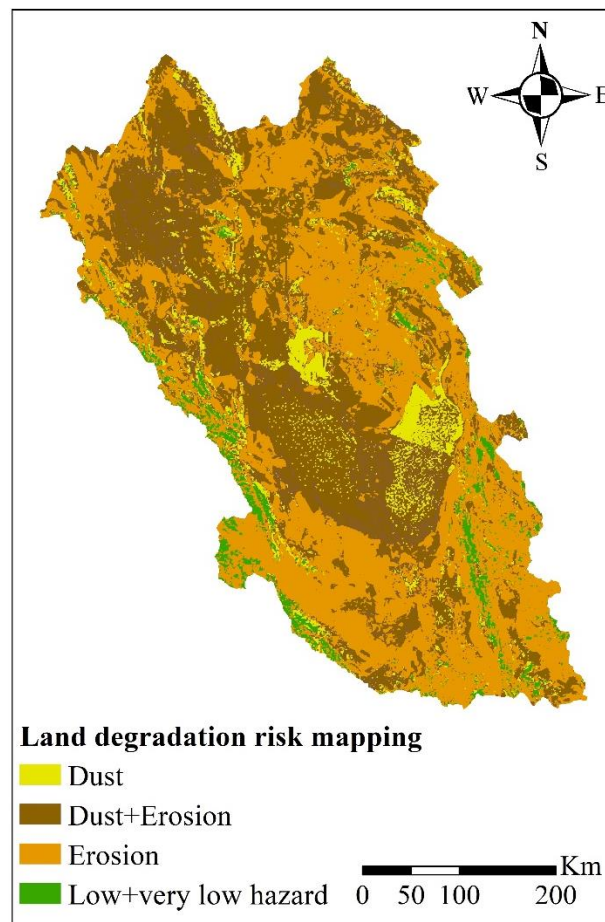
471 Fig. 6 soil erosion susceptibility areas map (GESM) using random forest (RF), artificial neural network
 472 (ANN), and flexible discriminate analyses (FDA)

473

474 3.3. Land degradation susceptibility

475 The majority of the study watershed is susceptible to a substantial risk for land
 476 degradation. The spatial distribution of land degradation susceptibility, shown in Fig.
 477 7, indicates that only 4% of the land area has low to very low risks of land degradation.
 478 Areas susceptible to both soil erosion by water and winds together constitute 43% of

479 the total area. Approximately 45% and 8% of the study area are at risk of soil erosion
480 by water and wind, respectively. Taken together, it means that the majority of the Lut
481 watershed falls under the category of land degradation risks. The watershed accounts
482 for 12.5% of the total land of Iran. The findings of the present study are therefore
483 consistent with a report that indicated water erosion as an environmental hazard in Iran
484 (Bui et al. 2019). The results of the study will be helpful and applicable for identifying
485 water-induced and dust sources hotspots across the watershed and prioritizing
486 appropriate conservation measurements and rehabilitative policies.
487 The areas that fall under the category of both kind of land degradation might be most
488 vulnerable concerning local self-sufficiency for food security and sustainability of
489 human activities. For instance, dust storms drive water loss through failure of
490 agricultural crops in Iran (Boroughani et al. 2022). Moreover, the adverse impacts of
491 water-induced soil erosion are known from numerous other regions (Lal and
492 Moldenhauer 2008, Gao et al. 2015, Standardi et al. 2018; Roy et al., 2022).



493
494
495

Fig. 7 Land degradation susceptibility map in terms of soil erosion and dust sources areas

496 **Conclusion**

497 Investigation of soil erosion through water along with wind-driven soil erosion from
498 dust sources have received little attention in past studies, despite their importance for
499 land degradation with associated social, economic, and environmental impacts. The
500 present study used several different data sets, conducted a field survey and paired the
501 data with three different machine learning algorithms to construct spatial maps for areas
502 of risk for land degradation for the Lut watershed in Iran. Three machine learning
503 algorithms were successfully applied to create land susceptibility maps describing dust
504 aerosol occurrence considering methodological uncertainty. In addition, these models
505 were used to identify the areas prone to soil erosion by surface water runoff. These
506 obtained maps were synthesized to generate a single map for risks of land degradation.
507 The results of the present study show that the random forest algorithm outperformed
508 the other two machine learning approaches for both dust sources and soil erosion
509 susceptibility mapping with an accuracy of 75% and 94%, respectively.
510 As expected, the vegetation cover, elevation, land use, and geology were important
511 prerequisites for dust-emission occurrence in the watershed, while rainfall,
512 Topographical Wetness Index (TWI), terrain slope, terrain elevation, land use, and
513 geology were identified as the most influential factors for water-induced soil erosion.
514 Based on the land degradation map, almost the entire study region is at risk. A large
515 fraction of 43% of the area is prone to both high wind-driven plus water-driven soil
516 erosion. In addition to these areas, another 45% and 8% of the area have a risk for water-
517 driven and wind-driven soil erosion, respectively. The methods tested in this study
518 could be later transferred to similar assessments in other regions around the world.
519 Choosing this region in Iran is further motivated by the impact of land degradation on
520 the country's economy. The current study has some limitation including the small
521 sample size and non-uniform distribution of water-induced soil erosion points because
522 of lack of accessibility to a road network in some parts of the watershed. Despite these
523 limitations, these results can potentially be useful for managers and policy makers to
524 identify local hotspots for land degradation to implement mitigation and adaptation
525 measures in this watershed. Future studies could work on improving the spatial
526 resolution and coverage of the risk assessment for providing more information on risks
527 for land degradation. In addition, it is suggested that future research should estimate the
528 role of other climatic factors such as humidity, and air temperature on soil erosion and
529 dust source susceptibility. Prediction of NDVI and rainfall as the most effective factors

530 on soil erosion and dust sources and estimated of their impacts on future water induced-
531 soil erosion and dust sources susceptibility is also suggested for the other studies. It
532 requires more measurements for soil erosion by water and winds to train the machine
533 learning models.

534

535 **Acknowledgement**

536 SF acknowledges funding from the German Research Foundation (DFG) for SFB
537 1502/1–2022 (Project: 450058266).

538

539 **Conflict of Interest**

540 The authors declare that there is no conflict of interests regarding the publication of
541 this article.

542

543 **References**

544 Amiri M, Pourghasemi HR, Ghanbarian GA, Afzali SF (2019) Assessment of the importance
545 of gully erosion effective factors using Boruta algorithm and its spatial modeling and mapping
546 using three machine learning algorithms. *Geoderma* 340:55–69.
547 <https://doi.org/10.1016/j.geoderma.2018.12.042>

548 Anache JAA, Flanagan DC, Srivastava A, Wendland EC (2018) Land use and climate change
549 impacts on runoff and soil erosion at the hillslope scale in the Brazilian Cerrado. *Science of the*
550 *Total Environment* 622–623:140–151. <https://doi.org/10.1016/j.scitotenv.2017.11.257>

551 Arabameri A, Chen W, Loche M, et al (2019a) Comparison of machine learning models for
552 gully erosion susceptibility mapping. *Geoscience Frontiers*.
553 <https://doi.org/10.1016/j.gsf.2019.11.009>

554 Arabameri A, Pradhan B, Rezaei K (2019b) Gully erosion zonation mapping using integrated
555 geographically weighted regression with certainty factor and random forest models in GIS.
556 *Journal of Environmental Management* 232:928–942.
557 <https://doi.org/10.1016/j.jenvman.2018.11.110>

558 Avand M, Moradi HR, Lasbooye MR (2021) Spatial prediction of future flood risk: An
559 approach to the effects of climate change. *Geosciences (Switzerland)* 11:1–20.
560 <https://doi.org/10.3390/geosciences11010025>

561 Beven KJ, Kirkby MJ (1979) A physically based, variable contributing area model of basin
562 hydrology/Un modèle à base physique de zone d'appel variable de l'hydrologie du bassin
563 versant. *Hydrological sciences journal* 24:43–69

564 Boroughani M, Mohammadi M, Mirchooli F, Fiedler S (2022) Assessment of the impact of
565 dust aerosols on crop and water loss in the Great Salt Desert in Iran. *Computers and Electronics*

566 in Agriculture 192:106605

567 Boroughani, M., Pourhashemi, S., Gholami, H., & Kaskaoutis, D. G. 2021. Predicting of dust
568 storm source by combining remote sensing, statistic-based predictive models and game theory
569 in the Sistan watershed, southwestern Asia. *Journal of Arid Land*, 13(11), 1103-1121.

570

571 Boroughani M, Pourhashemi S (2020) Susceptibility Zoning of Dust Source Areas by Data
572 Mining Methods over Khorasan Razavi Province. *Quarterly journal of Environmental Erosion*
573 *Research* 9:1–22

574 Boroughani M, Pourhashemi S, Hashemi H, et al (2020) Application of remote sensing
575 techniques and machine learning algorithms in dust source detection and dust source
576 susceptibility mapping. *Ecological Informatics* 56:101059.
577 <https://doi.org/10.1016/j.ecoinf.2020.101059>

578 Breiman L (2001) Random forests. *Machine Learning* 45:5–32.
579 <https://doi.org/10.1023/A:1010933404324>

580 Bui DT, Shirzadi A, Shahabi H, et al (2019) A novel ensemble artificial intelligence approach
581 for gully erosion mapping in a semi-arid watershed (Iran). *Sensors (Switzerland)* 19:.
582 <https://doi.org/10.3390/s19112444>

583 Chicas SD, Omine K, Ford JB (2016) Identifying erosion hotspots and assessing communities
584 'perspectives on the drivers , underlying causes and impacts of soil erosion in Toledo 's Rio
585 Grande Watershed : Belize. *Applied Geography* 68:57–67.
586 <https://doi.org/10.1016/j.apgeog.2015.11.010>

587 Darvand S, Khosravi H, Keshtkar H, et al (2021) Comparison of machine learning models to
588 prioritize susceptible areas to dust production. *Journal of Range and Watershed Managment*
589 74:53–68

590 Derakhshan-Babaei F, Mirchooli F, Mohammadi M, et al (2022) Tracking the origin of trace
591 metals in a watershed by identifying fingerprints of soils, landscape and river sediments.
592 *Science of The Total Environment* 155583

593 Ebrahimi-khusfi Z, Taghizadeh-mehrjardi R, Mirakbari M (2021) Evaluation of machine
594 learning models for predicting the temporal variations of dust storm index in arid regions of
595 Iran. *Atmospheric Pollution Research* 12:134–147. <https://doi.org/10.1016/j.apr.2020.08.029>

596 Emadodin I, Narita D, Rudolf H (2012) Soil degradation and agricultural sustainability : an
597 overview from Iran. *Environment, Development and Sustainability* 14:611–625.
598 <https://doi.org/10.1007/s10668-012-9351-y>

599 Gao L, Bowker MA, Xu M, et al (2017) Biological soil crusts decrease erodibility by modifying
600 inherent soil properties on the Loess Plateau, China. *Soil Biology and Biochemistry* 105:49–
601 58. <https://doi.org/10.1016/j.soilbio.2016.11.009>

602 Gao X, Xie Y, Liu G, et al (2015) Effects of soil erosion on soybean yield as estimated by
603 simulating gradually eroded soil profiles. *Soil and Tillage Research* 145:126–134

604 Garosi Y, Sheklabadi M, Conoscenti C, et al (2019) Assessing the performance of GIS- based
605 machine learning models with different accuracy measures for determining susceptibility to
606 gully erosion. *Science of the Total Environment* 664:1117–1132.
607 <https://doi.org/10.1016/j.scitotenv.2019.02.093>

608 Gholami H, Kordestani MD, Li J, et al (2019a) Diverse sources of aeolian sediment revealed
609 in an arid landscape in southeastern Iran using a modified Bayesian un-mixing model. *Aeolian*
610 *Research* 41:100547

611 Gholami H, Mohamadifar A, Sorooshian A, Jansen JD (2020a) Machine-learning algorithms
612 for predicting land susceptibility to dust emissions : The case of the Jazmurian Basin , Iran.
613 *Atmospheric Pollution Research* 11:1303–1315. <https://doi.org/10.1016/j.apr.2020.05.009>

614 Gholami H, Mohammadifar A, Collins AL (2019b) Spatial mapping of the provenance of storm
615 dust: Application of data mining and ensemble modelling Hamid. *Atmospheric Research*
616 104716. <https://doi.org/10.1016/j.atmosres.2019.104716>

617 Gholami H, Mohammadifar A, Pourghasemi HR, Collins AL (2020b) A new integrated data
618 mining model to map spatial variation in the susceptibility of land to act as a source of aeolian
619 dust. *Environmental Science and Pollution Research* 27:42022–42039

620 Ghorbanzadeh O, Kamran KV, Blaschke T, et al (2019) Spatial Prediction of Wildfire
621 Susceptibility Using Field Survey GPS Data and Machine Learning Approaches. *fire* 2:1–23

622 Gia T, Degener J, Kappas M (2018) Integrated universal soil loss equation (USLE) and
623 Geographical Information System (GIS) for soil erosion estimation in A Sap basin : Central
624 Vietnam. *International Soil and Water Conservation Research* 6:99–110.
625 <https://doi.org/10.1016/j.iswcr.2018.01.001>

626 Halecki W, Kruk E, Ryzek M (2018) Land Use Policy Loss of topsoil and soil erosion by
627 water in agricultural areas : A multi- criteria approach for various land use scenarios in the
628 Western Carpathians using a SWAT model. *Land Use Policy* 73:363–372.
629 <https://doi.org/10.1016/j.landusepol.2018.01.041>

630 Hosseinalizadeh M, Kariminejad N, Rahmati O, et al (2019) How can statistical and artificial
631 intelligence approaches predict piping erosion susceptibility? *Science of the Total Environment*
632 646:1554–1566. <https://doi.org/10.1016/j.scitotenv.2018.07.396>

633 Hahnenberger, M., Nicoll, K., 2014. Geomorphic and land cover identification of dust sources
634 in the eastern Great Basin of Utah, U.S.A. *Geomorphology* 204 (2), 657–672.
635 <https://doi.org/10.1016/j.geomorph.2013.09.013>.

636 Jafari M, Mesbahzadeh T, Masoudi R, et al (2021) Dust storm surveying and detection using
637 remote sensing data, wind tracing, and atmospheric thermodynamic conditions (case study:
638 Isfahan Province, Iran). *Air Quality, Atmosphere & Health* 1–11

639 Kalantar B, Pradhan B, Naghibi SA, et al (2017) Assessment of the effects of training data
640 selection on the landslide susceptibility mapping: a comparison between support vector
641 machine (SVM), logistic regression (LR) and artificial neural networks (ANN). *Geomatics,*
642 *Natural Hazards and Risk* 5705:1–21. <https://doi.org/10.1080/19475705.2017.1407368>

643 Kalantar B, Ueda N, Saeidi V, et al (2020) Landslide susceptibility mapping: Machine and
644 ensemble learning based on remote sensing big data. *Remote Sensing* 12:1–23.
645 <https://doi.org/10.3390/rs12111737>

646 Kim JW, Kim HG (2021) Landslide susceptibility analysis by type of cultural heritage site
647 using ensemble model: Case study of the Chungcheong Region of South Korea. *Sensors and*
648 *Materials* 33:3819–3833. <https://doi.org/10.18494/SAM.2021.3593>

649 Lal R, Moldenhauer WC (2008) Effects of soil erosion on crop productivity. *Effects of soil*
650 *erosion on crop productivity* 5:303–367. <https://doi.org/10.1080/07352688709382244>

651 Lee S, Hong S-M, Jung H-S (2017) GIS-based groundwater potential mapping using artificial
652 neural network and support vector machine models: the case of Boryeong city in Korea.
653 *Geocarto International* 6049:1–15. <https://doi.org/10.1080/10106049.2017.1303091>

654 Lee, J. A., Gill, T. E., Mulligan, K. R., Acosta, M. D., Perez, A. E. 2009. Land use/land cover
655 and point sources of the 15 December 2003 dust storm in southwestern North
656 America. *Geomorphology*, 105(1-2), 18-27

657 Mirchooli F, Motevalli A, Pourghasemi HR, et al (2019) How do data-mining models consider
658 arsenic contamination in sediments and variables importance? *Environmental Monitoring and*
659 *Assessment* 191:. <https://doi.org/10.1007/s10661-019-7979-x>

660 Mosavi A, Golshan M, Janizadeh S, et al (2020) Ensemble models of GLM, FDA, MARS, and
661 RF for flood and erosion susceptibility mapping: a priority assessment of sub-basins. *Geocarto*
662 *International*. <https://doi.org/10.1080/10106049.2020.1829101>

663 Naghibi SA, Ahmadi K, Daneshi A (2017) Application of Support Vector Machine, Random
664 Forest, and Genetic Algorithm Optimized Random Forest Models in Groundwater Potential
665 Mapping. *Water Resources Management* 31:2761–2775. <https://doi.org/10.1007/s11269-017->
666 1660-3

667 Park S, Kim J, Lee J, et al (2014) Combined dust detection algorithm by using MODIS infrared
668 channels over East Asia. *Remote Sensing of Environment* 141:24–39.
669 <https://doi.org/10.1016/j.rse.2013.09.019>

670 Péré J-C, Rivellini L, Crumeyrolle S, et al (2018) Simulation of African dust properties and
671 radiative effects during the 2015 SHADOW campaign in Senegal. *Atmospheric Research*
672 199:14–28

673 Rahmati O, Mohammadi F, Saeid S, et al (2020) Identifying sources of dust aerosol using a
674 new framework based on remote sensing and modelling. *Science of the Total Environment*
675 737:139508. <https://doi.org/10.1016/j.scitotenv.2020.139508>

676 Rahmati O, Pourghasemi HR, Melesse AM (2016) Application of GIS-based data driven
677 random forest and maximum entropy models for groundwater potential mapping: A case study
678 at Mehran Region, Iran. *Catena* 137:360–372. <https://doi.org/10.1016/j.catena.2015.10.010>

679 Roy J, Saha S (2019) GIS-based Gully Erosion Susceptibility Evaluation Using Frequency
680 Ratio , Cosine Amplitude and Logistic Regression Ensembled with fuzzy logic in Hinglo River
681 Basin , India. *Remote Sensing Applications: Society and Environment* 15:100247.
682 <https://doi.org/10.1016/j.rsase.2019.100247>

683 Sakizadeh M, Mirzaei R, Ghorbani H (2017) Support vector machine and artificial neural
684 network to model soil pollution : a case study in Semnan Province , Iran. *Neural Computing
685 and Applications* 28:3229–3238. <https://doi.org/10.1007/s00521-016-2231-x>

686 Shi P, Yan P, Yuan Y, Nearing MA (2004) Wind erosion research in China: Past, present and
687 future. *Progress in Physical Geography* 28:366–386.
688 <https://doi.org/10.1191/0309133304pp416ra>

689 Shit PK, Pourghasemi H reza, Bhunia GS (2020) Gully Erosion Studies from India and
690 Surrounding Regions

691 Standardi G, Panagos P, Montanarella L, et al (2018) Cost of agricultural productivity loss due
692 to soil erosion in the European Union : From direct cost evaluation approaches to the use of
693 macroeconomic models. *Land Degradation & Development* 29:471–484.
694 <https://doi.org/10.1002/ldr.2879>

695 Sun W, Shao Q, Liu J, Zhai J (2014) Assessing the effects of land use and topography on soil
696 erosion on the Loess Plateau in China. *Catena* 121:151–163.
697 <https://doi.org/10.1016/j.catena.2014.05.009>

698 Tehrany MS, Pradhan B, Jebur MN (2014) Flood susceptibility mapping using a novel
699 ensemble weights-of-evidence and support vector machine models in GIS. *Journal of
700 Hydrology* 512:332–343. <https://doi.org/10.1016/j.jhydrol.2014.03.008>

701 Yang M, Zhu X, Pan H, et al (2019) Changes of the relationship between spring sand dust
702 frequency and large-scale atmospheric circulation. *Atmospheric Research* 226:102–109.
703 <https://doi.org/10.1016/j.atmosres.2019.04.004>

704 Youssef AM, Pourghasemi HR (2021) Landslide susceptibility mapping using machine
705 learning algorithms and comparison of their performance at Abha Basin, Asir Region, Saudi
706 Arabia. *Geoscience Frontiers* 12:639–655

707 Zabihi M, Mirchooli F, Motevalli A, et al (2018) Spatial modelling of gully erosion in
708 Mazandaran Province, northern Iran. *Catena* 161:1–13.
709 <https://doi.org/10.1016/j.catena.2017.10.010>

710 Zerihun M, Mohammedyasin MS, Sewnet D, et al (2018) Assessment of soil erosion using
711 RUSLE, GIS and remote sensing in NW Ethiopia. *Geoderma Regional* 12:83–90.
712 <https://doi.org/10.1016/j.geodrs.2018.01.002>

713 Vickery, K., Eckardt, F. 2013. Dust emission controls on the lower Kuiseb River valley, central
714 Namib. *Aeolian Res.* 10, 125–133. <https://doi.org/10.1016/j.aeolia.2013.02.006>.
715 Walker, A.L., Liu, M., Miller, S.D., Richardson, K.A., Westphal, D.L., 2009. Development of
716 a dust source database for mesoscale forecasting in Southwest Asia. *J. Geophys. Res.* 114 (18),
717 1–24. <https://doi.org/10.1029/2008JD011541>.